

# Isometric Torque Values About Robotic Knee Using Braided Pneumatic Actuators

**Ben Bolen<sup>1,\*</sup>, Lindie Burgess<sup>1</sup>, Connor Morrow<sup>1</sup>, Mohamad Elzein<sup>1</sup>, Lawrence Pang<sup>1</sup>, Cody Scharzenberger<sup>1</sup>, and Alex Hunt<sup>1</sup>**

<sup>1</sup>Agile and Adaptive Robotics Laboratory, Portland State University, Department of Mechanical and Materials Engineering, Portland, OR, USA

Correspondence\*:

Ben Bolen  
 Portland State University  
 Department of Mechanical and Materials Engineering  
 PO Box 751  
 Portland, OR, 97207-0751, USA  
 bbolen83@gmail.com

ave their other characteristics?  
 might just say length chw  
 BPA Muscle

## 2 ABSTRACT

Artificial muscles such as braided pneumatic actuators (BPAs) offer many advantages for robotic systems, including high durability and strength-to-weight ratios. However, their use in robotic systems is still extremely limited, in part due to **their poor characterization, especially with regard to their force and length capabilities**. In this work, test setups are created to compare forces and torques produced by Festo fluidic BPAs with leading models. A ~~muscle force~~ setup was developed to test linear force while a robotic system of the lower limb of a bipedal humanoid robot was designed to test isometric torque values. Predicted torque values based on developed models are compared with recorded torque data to determine the major sources of error in current modeling tools. Our analysis of the data has resulted in 1) the development of new equations to calculate force as functions of pressure and contraction for Festo BPAs with diameters ( $\phi$ ) of 10 mm and 20 mm, 2) a novel equation for the maximum force in the 10 mm and 20 mm diameter Festo BPAs as a function of their resting length ( $l_{rest}$ ), 3) an improved model that includes a constant length offset and series spring elements, and 4) a correction factor for when the BPAs wrap around joints to account for the loss in usable length. Finally, we show that Festo BPAs can meet or exceed human maximum isometric knee torque values over a majority of the knee range of motion (RoM). This work demonstrates a greatly improved model that is better able to predict joint torques produced by Festo BPAs in biomimetic designs. This will lead to faster design processes and the development of biomimetic robots that are able to more accurately reproduce the range of motion and isometric torque profiles that exist in the animals they are mimicking.

**Keywords:** BPA, Biomimetic, Function Fit, PAM, Artificial Muscle, Bioinspired, Bipedal Robot, Isometric Knee Torque

## 1 INTRODUCTION

Biomimetic robots offer many potential applications ranging from assisting in factories, exploration, and even understanding our own bodies. By developing high-fidelity biomimetic robots, we can perform tests that help improve our understanding of both biomechanics and the underlying neuromechanical systems

embellish  
a bit

present  
us post  
model  
what?

that control them (Shin et al., 2018; Asano et al., 2019; Ijspeert, 2020; Goldsmith et al., 2021; Hunt et al., 2017b; Schilling et al., 2022). With these robotic systems, experiments can be performed that would not be practical or ethical if done on human test subjects, such as turning off part of the neural control system or removing specific muscles. Such tests allow direct testing of how different components of the neuromechanical system interact. These robotic platforms offer new opportunities for testing neural control theories that are not currently possible, and are potentially faster and cheaper than human observation studies.

Biomimetic robots built with artificial muscles provide opportunities to investigate how muscles are controlled to produce desired motions. There are biomimetic robots that are actuated with artificial muscle, such as the impressive Kengoro and Kenshiro robots designed by Asano et al. (Asano et al., 2017, 2019). These muscles use brushless DC motors, wires, gears, and integrated tension measurement devices. There is also the puppy robot actuated with Festo BPAs, designed by Hunt(Hunt et al., 2017a). McKibben style BPAs (also called Pneumatic Artificial Muscles or PAMs) have low weight, high force/weight ratio, high efficiency, and a force-length curve that is similar to actual muscle. Combining these artificial muscles with muscle control schemes that have been developed using muscle models in simulation can allow more effective investigations of dynamic interactions with the environment than current physics simulators have to offer (Hunt et al., 2017b). Unfortunately, artifical muscles do not exactly replicate muscle properties, which has made it difficult to build a robot that is capable of capturing all the degrees of freedom and joint torques of human limbs.

Previous research has worked to bridge this gap through the development of higher-fidelity artificial muscle models. Festo provides a tool that can predict the force produced by their actuators at different lengths and different pressures (Lang, 2005). However, analysis of experimental data indicates that this tool does not effectively take into account differences in force due to initial actuator length and total contraction ability. To address this issue, a more accurate force-pressure-length model of  $\phi 10$  mm Festo BPAs was developed that incorporates changes that occur due to different amounts of maximum contraction found in BPAs (Hunt et al., 2017a). In this work, we have further developed this model by taking data at a significant number of lengths and at higher forces for both 10 mm and 20 mm muscles. *Is it possible that this model or experimental setup could be used for other types of PAMs? Broaden the application?*

In addition to problems caused by inaccurate artificial muscle models, it is unknown how different attachment locations and interactions between the artificial muscles and other components affect torques produced on the robot. Previous work modeled how the location of muscle attachments affects the torque capabilities of each muscle and compared these capabilities with human data and determined that if artificial muscles are placed in the same locations as human muscles, the developed robot will not be able to achieve the same range of motion (RoM) or torque that humans achieve (Bolen and Hunt, 2019). To improve the range of motion and torque generated by the BPAs, optimization methods were developed that find attachment locations that can produce a torque curve and range of motion that match human capabilities (Morrow et al., 2020). However, bending and kinking of the artificial muscle as it wraps around a joint could reduce the force produced by the muscle. Joint friction can cause a decrease in torque, as can non-rigid elements of the artificial leg. Therefore, the work presented here also seeks to understand how much of an effect these interactions have on joint torque and build in correction factors that can improve modeling methods.

In summary, this work sets out to fill in these modeling gaps by developing a better model of force produced by  $\phi 10$  mm Festo BPAs, and extending this model to  $\phi 20$  mm Festo BPAs, which are needed to produce the high torques found about the human knee joint. In addition, an isometric knee test stand was created to allow measurements of the torque about the knee joint in various configurations. Data

70 collected from the test stand are compared with theoretical torque values, and is used to develop an  
 71 improved model that incorporates losses due to compliance. This work also demonstrates that the improved  
 72 attachment locations produced by the optimization method in previous work (Morrow et al., 2020) are  
 73 cable of producing torques that match or exceed human capabilities across a wide range of joint angles.

## 2 METHODS AND MATERIALS

### 74 2.1 Overview

75 This study begins with building a jig to measure artificial muscle force as a function of length and pressure.  
 76 Festo BPAs of 10 mm and 20 mm diameter were tested with various resting lengths and different amounts  
 77 of contraction. These data are used to develop an improved model that more accurately predicts maximum  
 78 muscle force based on  $l_{rest}$ , current muscle length  $l_m$ , and pressure  $P$ . A second jig was constructed to  
 79 test the torque produced by these artificial muscles about a knee joint. With the expectation that measured  
 80 torque will be less than that predicted by the model, the robot muscle arrangement and knee design are  
 81 simplified to elucidate the variables that most affect the results. Two distinct joints are used and tested: a  
 82 simplified pinned knee joint and a biomimetic knee (Steele, 2018). Each joint is driven by a single flexor  
 83 and a single extensor muscle. Variations were made to muscle origin/insertion locations, resting lengths,  
 84 diameters, and whether they used an artificial tendon. The results are compared with two models and the  
 85 new data was used to create an updated robot model.

### 86 2.2 Previous Actuator Force Model

87 Previous studies have generated empirical models of the force-length-pressure relationship of BPA  
 88 actuators. Sarosi et al. discuss several high-fidelity BPA force models (Sárosi et al., 2017). They present  
 89 a static force model with a 21 coefficient polynomial function for a Festo MAS-20-200N (i.e.  $\phi 20$  mm,  
 90  $l_{rest} = 200$  mm) with an impressive  $R^2 = 0.9994$ . They also present Sarosi's static force model for a  
 91 Festo DMSP-20-400N-RM-RM (i.e.  $\phi 20$  mm,  $l_{rest} = 400$  mm), with 6 coefficients and an  $R^2 = 0.9995$ .  
 92 Martins and Boblan present an even more accurate model, in terms of absolute error, using five coefficients  
 93 for a DMSP-10-250 (i.e.  $\phi 10$  mm,  $l_{rest} = 250$  mm) and a DMSP-20-300 (i.e.  $\phi 20$  mm,  $l_{rest} = 300$  mm)  
 94 (Martens and Boblan, 2017). These models work well as long as the initial resting actuator length is the one  
 95 described in the papers, however different resting lengths produce different force-length curves, making it  
 96 impossible to compare all these results with the data we collected.

97 Hunt et al. looked at six resting lengths of  $\phi 10$  mm Festo BPAs, accounted for differences in maximum  
 98 contractile percentages, and elucidated the force-length-pressure relationship Hunt et al. (2017a). In  
 99 particular, for a given robot configuration and pressure  $P$  (in kPa), the scalar force  $F$  (in Newtons) for a  
 100  $\phi 10$  mm Festo artificial muscle can be determined by solving the equation:

$$P = 254 \text{ kPa} + 1.23 \frac{\text{kPa}}{\text{N}} \cdot F + 15.6 \text{ kPa} \cdot S +$$



$$192 \text{ kPa} \cdot \tan \left( 2.03 \left( \frac{\epsilon}{-0.331 \times 10^{-3} \frac{1}{\text{N}} \cdot F + \epsilon_{max}} - 0.46 \right) \right) \quad (1)$$

*One is full  
Lm & the other  
is not. Use (in N)?*

101 where  $S$  is the artificial muscle hysteresis factor such that  $S = 1$  indicates the muscle is shortening,  
 102  $S = -1$  indicates it is lengthening, and  $S = 0$  under static conditions. An important note for Eq. 1 is that  
 103 the coefficients have been updated with the correct values as the values reported in Hunt et al. (2017a)  
 104 contained typographical errors. The amount of contraction  $\epsilon$  is calculated as

*hehe, got 'em!*

$$\epsilon = \frac{(l_{rest} - l_m)}{l_{rest}} \quad (2)$$

105 and  $\epsilon_{max}$  is the maximum amount of contraction in a BPA without external load when inflated at 620 kPa  
 106 (90 PSI), similarly calculated as

*since mostly everything is in metric, is it more useful for english units here?*

$$\epsilon_{max} = \frac{(l_{rest} - l_{min})}{l_{rest}} \quad (3)$$

107 where  $l_{min}$  is defined as the muscle length measured at maximum contraction. Eq. 1 was used to create a  
 108 lookup table for actuator force,  $F$ , for a given amount of pressure,  $P$ , and relative contraction,  $\epsilon^*$ , defined  
 109 as

$$\epsilon^* = \frac{\epsilon}{\epsilon_{max}} \quad (4)$$

110 using the results from Eq. 2 and Eq. 3.

111 This model was taken at low forces ( $\leq 24$  lbs), and it is unclear how well this model captures actuator  
 112 behavior at higher forces, and so we compare this model with data collected in this work.

### 113 2.2.1 BPA force characterization experiment

114 A test jig was made of 80/20 brand 1515 series extruded aluminum (Fig. 1A). Artificial muscles were  
 115 placed vertically in the jig one at a time. The upper end was attached to an S-shaped load cell. The lower  
 116 end was attached to an adjustable crossmember that was used to change the actuator length  $l_m$ . Compressed  
 117 air was supplied through the building at 620 kPa and measured with a Freescale MPX5700 pressure sensor.

118 The inner distance between the hose clamps on each BPA was measured to determine the muscle's resting  
 119 length ( $l_{rest}$ ). This is how Festo defines  $l_{rest}$ , although in (Hunt et al., 2017a) it was measured to also  
 120 include end cap length. We then inflated each BPA to  $P_{max} = 620$  kPa, with one end allowed to move freely  
 121 in the axial Degree of Freedom (DoF), and measured the length  $l_{min}$  to calculate maximum contraction  
 122 using Eq. 3. The distance between the crossmembers was then controlled to get different amounts of  
 123 contraction, the muscles were inflated to various pressures, and the contractile force was recorded at the  
 124 pressure-contraction pairs. This was done for  $\phi 10$  mm BPA resting lengths ( $l_{rest}$ ) of 112 mm, 120 mm,  
 125 220 mm, 260 mm, 281 mm, 415 mm, 455 mm, 490 mm and 518 mm.

## 126 2.3 Isometric Knee Torque

### 127 2.3.1 Robot Model

128 The primary components of the robot leg are the knee joint, femur, tibia, BPA assemblies, and artificial  
 129 tendons (Fig. 1B–D). The artificial bone components are 3D printed using a combination of Onyx, carbon  
 130 fiber, and high-strength high-temperature fiberglass on Markforged Onyx One and Mark Two printers.

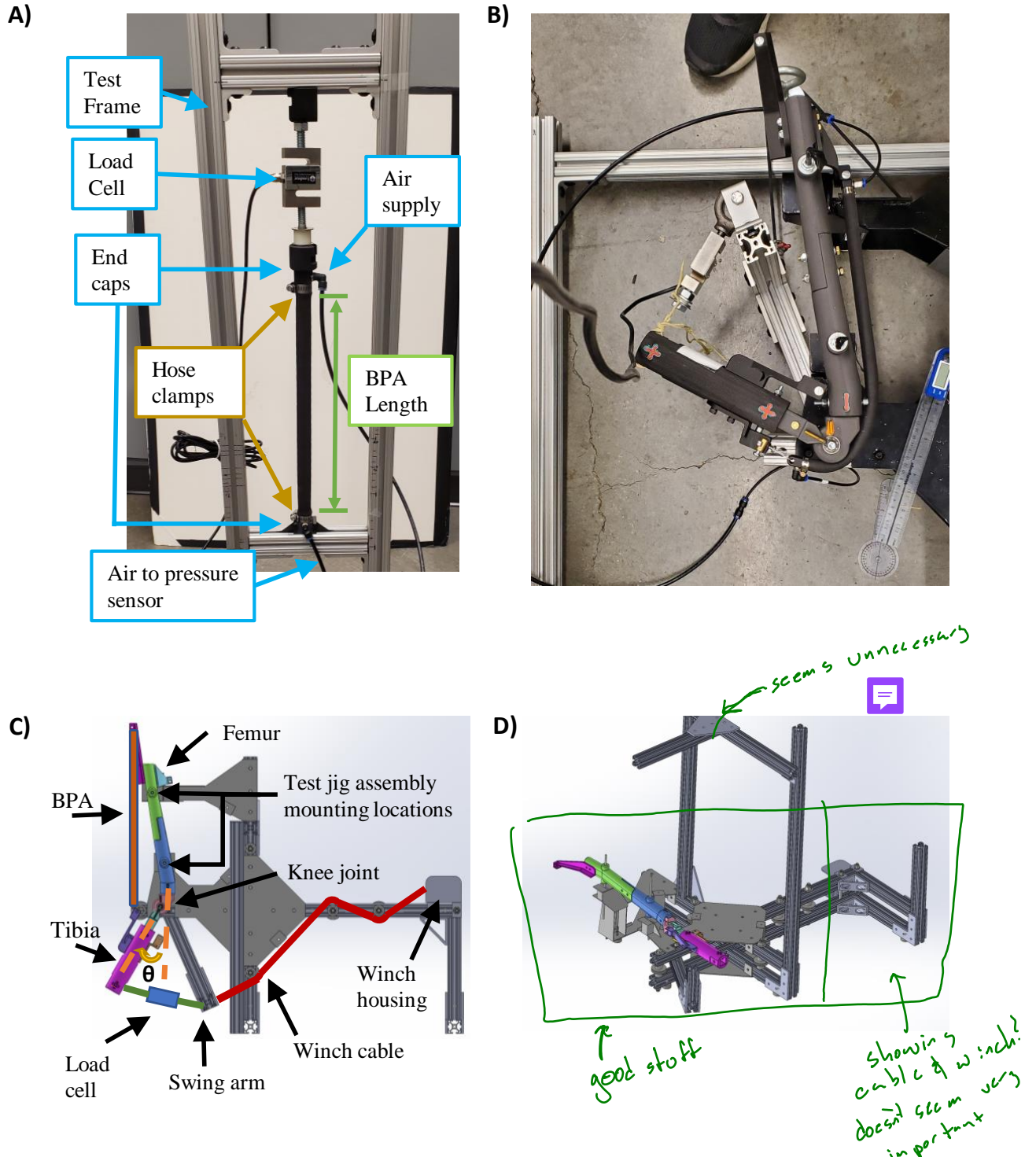


**Figure 1.** (A) A picture of a BPA in the isometric force test stand with components labeled. (B) Picture of robot leg in isometric torque test jig. Setup shows the pinned knee configured for a test of the extensor BPA. The knee is flexed with  $\theta_k = -120^\circ$ . The S shaped load cell attaches the tibia to the swing arm and is nearly perpendicular to the tibia in this configuration. Also note the compressed shape of the inflated BPA on the knee during this high degree of flexion.(C) 1-DoF pinned-joint robot knee in the test apparatus with important components labeled. Leg is shown with 30 degrees flexion, i.e.  $\theta_k = -30^\circ$ . (D) CAD solid model assembly of the revolute joint knee in the test stand.

131 Onyx is a proprietary Markforged material that consists of chopped carbon fiber in nylon. Artificial tendons  
 132 are made with Shimano bicycle brake cable.

133 The leg assembly geometry and dimensions are based on bones scans of a 6 ft (approximately 1.83 m)  
 134 tall person (Bolen and Hunt, 2019; Seth et al., 2018; Delp et al., 1990, 2007). Each joint is driven by  
 135 two antagonistic Festo actuators. Both robot joints have the same center of rotation in the femur frame at  
 136  $\theta_k = 0$  deg.

137 Details on the biomimetic robot knee used in this study can be found in Steele (2018); Steele et al. (2017,  
 138 2018). In brief, this 1-DoF joint uses a four-bar linkage to change the effective moment arm during rotation.  
 139 The intersection point of the internal crossed links define the instantaneous center of rotation (ICR). This  
 140 causes the joint ICR location in the femur frame to translate in the X and Y directions (Wu and Cavanagh,  
 141 1995; Wu et al., 2002) during knee rotation (see Figs. 1B and 1C), similar to how the human knee behaves  
 142 (Bolen and Hunt, 2019; Morrow et al., 2020; Seth et al., 2018; Delp et al., 2007, 1990).

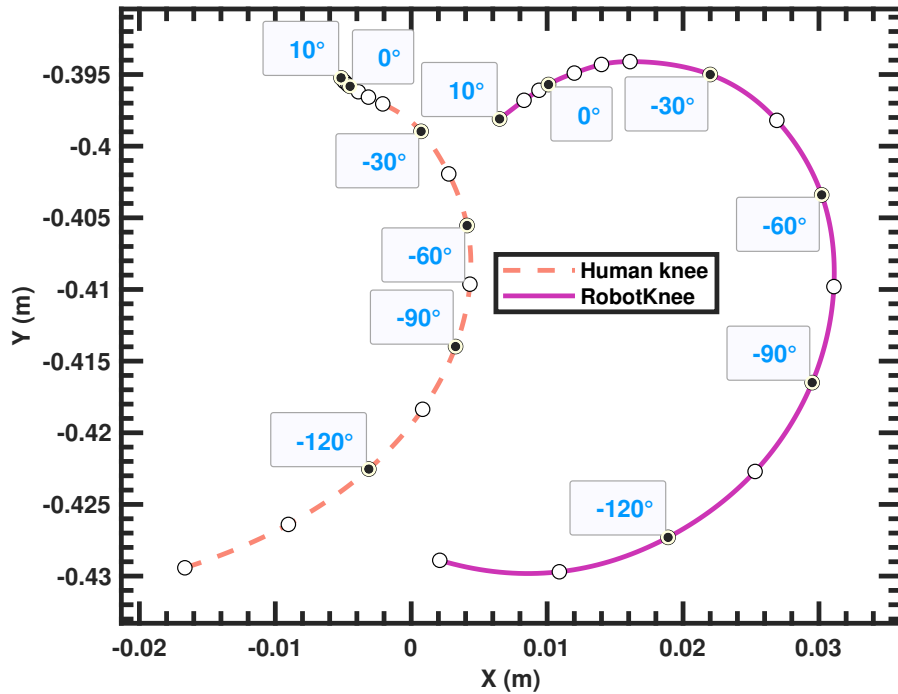


**Figure 2.** ICR for robot and human knee as a function of knee angle.

143 One uniarticular knee extensor and one uniarticular knee flexor are used to actuate the joint. Each knee  
 144 joint type is tested using  $\phi 10$  mm Festo BPAs. Additionally, the biomimetic knee joint was tested using a  
 145  $\phi 20$  mm Festo BPA. Each artificial muscle was pinned at the muscle origin location while the other end  
 146 was either pinned or attached to the muscle insertion location via an artificial tendon.

147 Moment arms are calculated using vector components between muscle locations and the joint center of  
 148 rotation. Given a vector  $\vec{d}$  from a joint to the line of action of the force vector  $\vec{F}$ , the moment arm  $\vec{r}$  is the  
 149 shortest distance to this line of action. In this study it is calculated using the method specified by Young  
 150 and colleagues (Young et al., 2019). The scalar moment arm,  $r_k$ , about the  $z_k$  axis (i.e. the Z axis in the  
 151 knee frame) is calculated as

$$r_k = p_{proj,xy} \cdot \frac{\vec{p_f} \times \hat{z}_k}{\|\vec{p_f} \times \hat{z}_k\|} \quad (5)$$

152 where  $p_{proj,xy}$  is the free muscle segment projected onto the  $XY$ -plane, which is normal to the joint axis.  
 153  $\vec{p_f}$  is the projected muscle segment vector. Moment arm is calculated in the tibial body frame.

154 Full details of the existing model and method to calculate torque in the modeled robot are in (Bolen and  
 155 Hunt, 2019; Morrow et al., 2020).

156 2.3.2 Knee Torque Data Collection

157 A test jig was built to collect knee torque measurements at different knee angles over its range of motion.  
 158 The test stand frame is made predominantly out of 80/20 1515 series extruded aluminum components.  
 159 The knee joint is free to rotate the tibia while the femur is fixed to the frame. A force sensor has one end  
 160 connected to the tibia and the other is connected to a swing arm. The swing arm is tied to a winch with  
 161 3/16 inch Kevlar rope from Quality™ Nylon Rope (see Fig. 1B and 1C). The knee joint is co-axial with  
 162 gravity to eliminate gravitational torque (Fig. 1D).

163 Force data was collected using one of two different sensors. The first is a MODERN STEP 300 kg digital  
 164 crane scale. The second force sensor is a CALT DYLY-103 100 kg S shaped load cell. The load cell is used  
 165 in conjunction with a HX711 Load Cell Amplifier. Pressure is measured with a Freescale MPX5700 GP  
 166 5 V pressure sensor. Building air supply pressure is controlled with two pressure regulators in series. The  
 167 first is a Parker model 20R113GC 0 – 120 psi pressure regulator. The second is a Husky 3/8 inch High  
 168 Performance Air Regulator HDA72200. A Festo VTUG-10-MRCR-S1T-26V20-T516LA-UL-T532S-8K  
 169 valve manifold was used to supply air to the actuator. Pressure and load cell amplifier data are sent to  
 170 Matlab via an Arduino Uno style Sparkfun BlackBoard C microcontroller.

171 The length measurements were made using a tape measure. When there was sufficient curvature in the  
 172 BPA during knee extensor torque tests, a flexible piece of string was used to mark the axial length and  
 173 then transferred to the tape measure. Angle measurements were taken with a Medigauge digital electronic  
 174 goniometer or with MALENOO analog goniometers of 6, 8, or 12 inch lengths.

175 2.3.3 Hybrid Torque Calculation Method

176 A Hybrid Torque calculation method was developed to help uncover inconsistencies between the model  
 177 and recorded torque values. This method measures the actual muscle length and angles of the robot to  
 178 predict force and joint torque. With this method, we are better able to determine which parts of the torque  
 179 equation did not achieve their predicted value and provide a correction to that part of the equation. The  
 180 classical mechanics way to calculate the torque  $\vec{M}$ , about a joint is to take the cross product of distance,  $\vec{d}$ ,  
 181 and force,  $\vec{F}$

$$\vec{M} = \vec{d} \times \vec{F} \quad (6)$$

182 where distance  $\vec{d}$  and force  $\vec{F}$  are described in the previous section. Knee torque is the scalar torque  $M$   
 183 about  $Z$ , which can be simplified Eq. 6 to

$$M = r \cdot F \quad (7)$$

184 where  $r$  is the moment arm measured by a tape measure, and  $F$  is the scalar force, calculated by  
 185 measuring the BPA's  $P$ ,  $l_{rest}$ ,  $l_{min}$  and  $l_m$  values and using the model fit equations determined in the  
 186 following section.

*↑ long sentence, consider breaking up. It harder how Hybrid torque method differs from classical method*

### 3 RESULTS

#### 187 3.1 Actuator Force

##### 188 3.1.1 Maximum Force

189 Data of the maximum force from BPA characterization tests of the 10 mm and 20 mm diameters show a  
 190 dependency on resting length (Fig. 3B). This is a previously unreported characteristic of these artificial  
 191 muscles. Detailed analysis of the Festo Tool (Festo, 2022), do in fact predict a change in maximum force  
 192 with the resting length, however the Festo Tool predicts increased force with shorter lengths, while our  
 193 collected data indicate decreasing force with shorter lengths. The data show a force response resembling an  
 194 arctan curve along the  $l_{rest}$  dimension. Using the Nonlinear Least Squares method and a Least Absolute  
 195 Residual robustness, we fit an arctan curve to the data at to get the maximum force given a resting length at  
 196 620 kPa as:

$$F_{max_{10}} = 303.5 \text{ N} \cdot \arctan(19.03 \text{ m}^{-1} \cdot (l_{rest} - 0.0075)) \quad (8)$$

$$F_{max_{20}} = 922.4 \text{ N} \cdot \arctan(15.37 \text{ m}^{-1} \cdot (l_{rest} - 0.013)) \quad (9)$$

197 The length is offset by 0.0075 m and 0.013 m because solid modeling showed that the end caps contact  
 198 each other at these lengths. At these lengths, the actuator would not be able to contract to produce force.

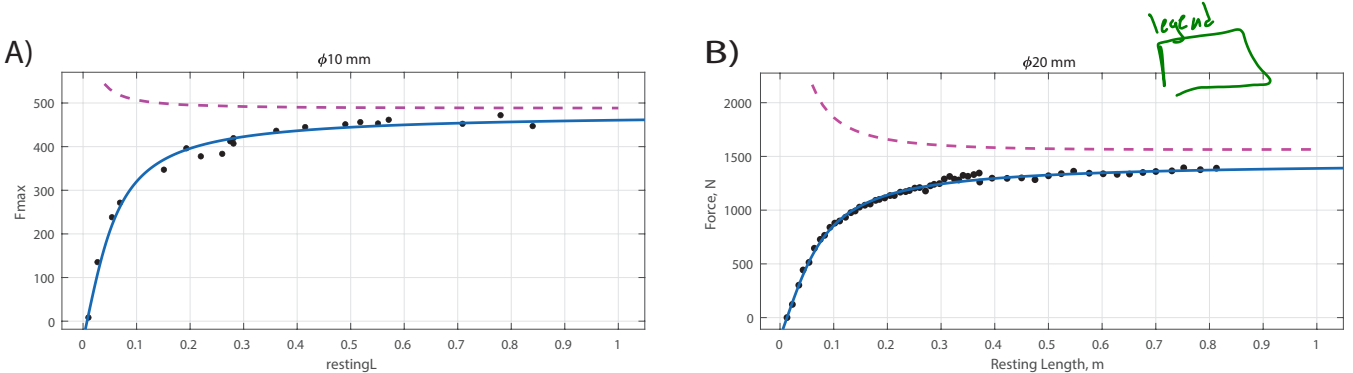


**Figure 3.** Results for finding the relationship between  $F_{max}$  and  $l_{rest}$ . **(A)**  $F_{max_{10}}$  as a function of  $l_{rest}$ , at  $P_{max} = 620 \text{ kPa}$ . Dashed line is the  $F_{max_{10}}$  data from Festo. Solid line is the fit from equation 8. **(B)**  $F_{max_{20}}$  as a function of  $l_{rest}$  at  $P_{max} = 620 \text{ kPa}$ . Dashed line is  $F_{max_{20}}$  data from Festo. Solid line is the fit from equation 9.

199 3.1.2 Force as a function of pressure

200 Data from BPA characterization tests of the 10 mm muscles resulted in force-pressure pairings for  
 201 different muscle resting lengths ( $l_{rest}$ ) Fig. 3A. Similar to the maximum force data, these data show a  
 202 force response resembling an arctan curve along the  $l_{rest}$  dimension and with a more linear response with  
 203 changes in pressure. Using the Nonlinear Least Squares method and a Least Absolute Residual robustness,  
 204 we fit an arctan curve to the data to get the maximum force given a resting length and pressure as:

$$F_{max}(l_{rest}, P) = a_1 \cdot P \cdot \arctan(a_2 \cdot P \cdot (l_{rest} - 0.0075)) \quad (10)$$

205 where  $a_1 = 0.4895 \text{ N kPa}^{-1}$  and  $a_2 = 0.03068 \text{ kPa}^{-1} \text{ m}^{-1}$  for the 10 mm actuator, and  $a_1 =$   
 206  $1.49 \text{ N kPa}^{-1}$ ,  $a_2 = 0.0248 \text{ kPa}^{-1} \text{ m}^{-1}$  for the 20 mm actuator. Goodness-of-fit measures are given  
 207 in Table 1 in the appendix.

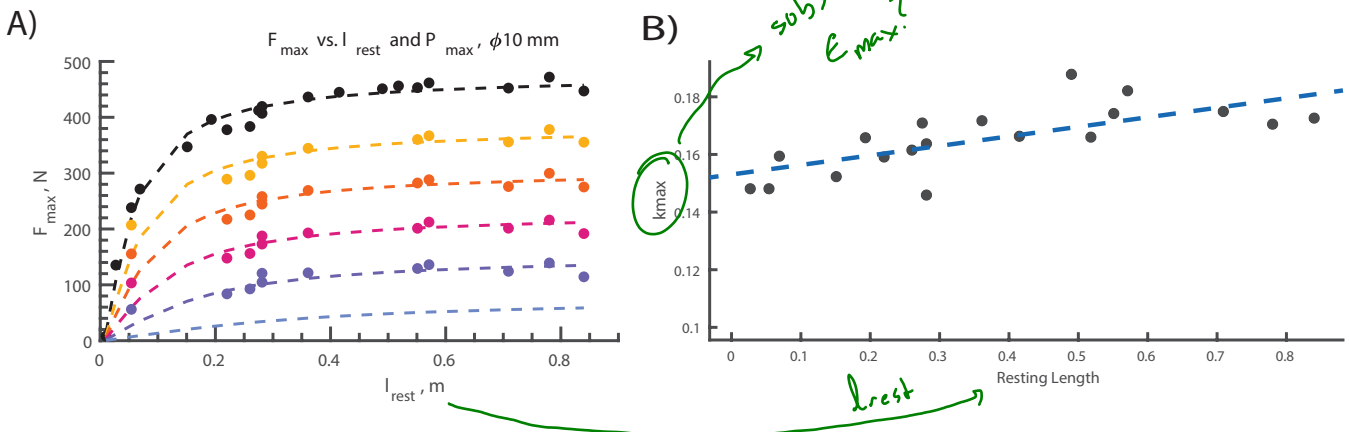


**Figure 4.** Results for finding the relationship between  $F_{max}$ ,  $l_{rest}$ ,  $P_{max}$ , and  $\epsilon_{max}$ . (A) Isoclines of the surface fit for  $F_{max10}(l_{rest}, P_{max})$ . (B)  $\epsilon_{max}$  versus  $l_{rest}$  at  $P_{max} = 620 \text{ kPa}$ . Although there is a general trend of longer resting lengths producing more contraction, no conclusive relationship between  $\epsilon_{max}$  and  $l_{rest}$  could be deduced from this experiment.

208 3.1.3 Maximum Contraction

*Capital when other sections are cut?*

209 Fig. 4B shows an attempt at a linear fit for maximum contraction ( $\epsilon_{max}$ ) as a function of resting length  
 210 ( $l_{rest}$ ). There was a large amount of variance in the data, with the linear fit giving an adjusted  $R^2 = 0.4124$   
 211 and an RMSE = 0.0083. Since there is no direct, predictable relationship between maximum contraction  
 212 and  $l_{rest}$ , this value should be recorded in each muscle used on a robot to best predict the force it may  
 213 produce at different pressures and contraction.

214 3.1.4 Force as a function of pressure and contraction

215 In addition to being a function of the pressure and resting length, the force produced by the actuator is  
 216 also a function of the amount of actuator contraction, with less force being applied as the actuator contracts.  
 217 The collected data of force, pressure, and contraction are normalized by dividing by  $F_{max}$ ,  $P_{max}$ , and  $\epsilon_{max}$ ,  
 218 respectively. This had the effect of compressing the data into a 3D surface ranging from 0 to 1 on all axes.  
 219 The normalized data are compared with pressure isoclines of force predicted by the Festo tool divided by  
 220 the maximum force equation described in the previous section (Fig. 5). With this comparison, it is clear that  
 221 the Festo tool over predicts the expected force, especially at lower pressures and contraction.

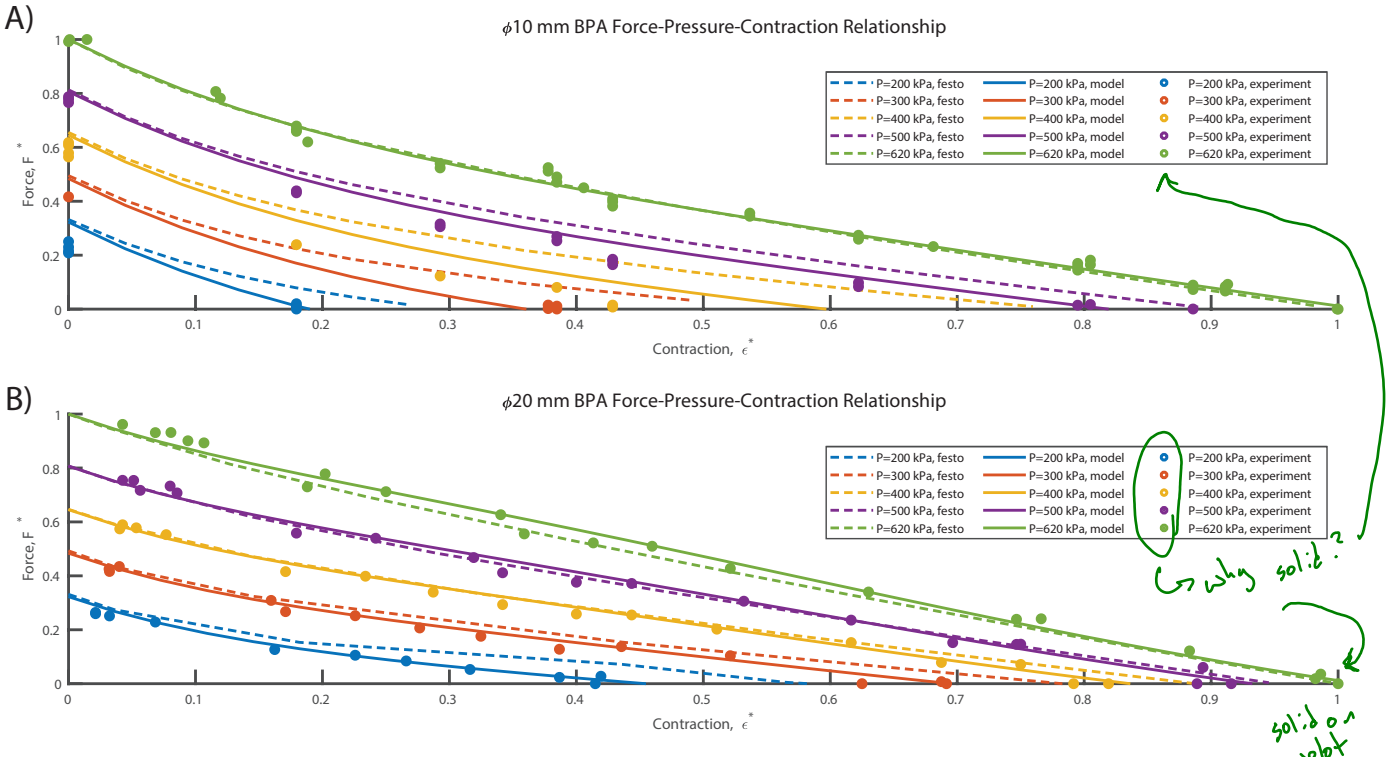


**Figure 5.** Surface fit for  $F^*(\epsilon^*, P^*)$ . Solid lines are from our model. Dashed lines from Festo supplied data. In total, XXX data points were collected and used to fit a 3D surface. For figure clarity, plotted circles represent collected data at  $\pm 10 \text{ kPa}$  isoclines of the stated pressure. **(A)** Fit data for  $\phi 10 \text{ mm}$  Festo BPAs. **(B)** Fit data for  $\phi 20 \text{ mm}$  Festo BPAs.

222 We therefore derived our own equation for isometric force in the BPA as a function of pressure and  
 223 contraction. Visual analysis of the experimental data shows an exponential relationship between  $\epsilon^*$  and  
 224  $F^*$ , and a linear relationship between  $P^*$  and  $F$ . We fit a surface to the original data using nonlinear least  
 225 squares and a least absolute residual robustness such that:

$$F^*(\epsilon^*, P^*) = \begin{cases} c_0 \cdot (\exp(-c_1 \cdot \epsilon^*) - 1) + P^* \cdot \exp(-c_2 \cdot \epsilon^{*2}) & F^* > 0 \\ 0 & F^* \leq 0 \end{cases} \quad (11)$$

226 For the  $\phi 10 \text{ mm}$  BPAs, the result of the improved fit can be seen in Figure 5A. The adjusted  $R^2 = 0.9998$ ,  
 227 a RMSE = 0.004537, and a maximum absolute residual of 10.6%. Solving 11 for the  $\phi 20 \text{ mm}$  BPA, yields  
 228 different coefficients, and results are seen in figure 5B. Coefficient values and goodness of fit statistics are  
 229 found in table 2.

### 230 3.2 Joint Torques

#### 231 3.2.1 Flexor on Pin Joint

232 Experimentally measured torque is compared with various prediction methods while using flexor BPAs  
 233 on the pinned knee joint (Fig. 6). These results show that the original model and improved BPA force  
 234 model over predict the measured torque at the knee for all joint angles, although the the improved model  
 235 performs slightly better (Fig. 6A and 6B). However, when the measured parameters ( $l_m$  and  $r_k$ ) are used in

236 the hybrid model, then predictions closely match the experimental data. This indicates that the kinematics  
 237 of the torque model are incorrectly predicting  $l_m$  and  $r_k$ .

238 Analysis of the measured data indicate that actual muscle length was consistently shorter than predicted  
 239 muscle length at all joint angles. This shorter length results in less muscle force, a shifted RoM, and less  
 240 torque in the experimental setup. That this shorter length occurs when  $\epsilon = 1$ , and  $F = 0$ , shows that a  
 241 constant length offset should be used. Therefore to produce an improved torque prediction model,  $l_m$  was  
 242 recalculated as

$$l_m = l_{LMT} - 2 l_{fitting} \quad (12)$$

243 where  $l_{LMT}$  is the path length of the musculotendon from origin to insertion point and  $l_{fitting}$  is the  
 244 length of the end caps.

245 Additionally, as the muscles produce more force, it causes parts in the limb segments to bend, causing  
 246 the muscle to shorten and produce less force. This is most apparent at high force and low contraction. To  
 247 correct this error, we modified Eq. 12 to be

$$l_m = l_{LMT} - 2 l_{fitting} - l_{tsl} - X_0 \quad (13)$$

248 where  $X_0$  is a constant length offset term. We then put a reference frame on superior posterior tibial  
 249 bracket bolt and drew a vector from there to the flexor insertion point. This vector is the  $X$  axis of this  
 250 frame, and the  $Y$  axis is pointed in the posterior direction with respect to the tibia frame. We then said  
 251 system compliance can be approximated by using an axial stiffness term  $X_1$  in the  $X$  direction, and a  
 252 bending stiffness term  $X_2$  in the  $Y$  direction. *Im not sure if this is an actual program?*

253 Multiobjective optimization using gamultiobj in Matlab was used to determine the length offset and  
 254 stiffness terms until the error between the the model and experimental data was minimized for the  $l_{rest} =$   
 255  $48.5\text{ cm BPA}$  (Fig. 6C).The solution yielded  $X_0 = 9\text{ mm}$ ,  $X_1 = 46.7\text{ kN m}^{-1}$ , and  $X_2 = 10.2\text{ kN m}^{-1}$ .  
 256 It can be seen that the model with these correction factors greatly improves the ability to predict the  
 257 joint torque, even capturing the reduction in force at small joint angles that was completely missing from  
 258 the previous model. The  $l_{rest} = 45.7\text{ cm BPA}$  was used for validation (Fig. 6C). It can be seen that the  
 259 improved model does a good job of predicting the torque with a different muscle length configured to  
 260 operate over a different joint range of motion. *nice.*

261 Error is defined as RMSE, FVU, and maximum absolute residual. Of all the Pareto front solutions, we  
 262 picked the one with the least distance between vectors using the goodness of fit objectives. The optimized  
 263 torque prediction for the  $l_{rest} = 48.5\text{ cm BPA}$  has an RMSE = 1.616, FVU = 0.0.0958, and a maximum  
 264 absolute residual of 3.2527. This is validated on the  $l_{rest} = 45.7\text{ cm BPA}$  which has an RMSE = 2.1214,  
 265 FVU = 0.0878, and a maximum absolute residual of 5.1690.

### 266 3.2.2 Extensor on Pin Joint

267 Pinned knee extensor results using  $\phi 10\text{ mm Festo BPAs}$  with  $l_{rest}$  values 48.0 cm, 45.7 cm and 41.5 cm  
 268 are shown in Fig. 7. Dashed black line shows the torque predicted with our original model. Blue dots are  
 269 the experimentally measured torque. Yellow dots represent the hybrid method of calculating torque by  
 270 experimentally measuring pressure, muscle length, and moment arm. These muscle lengths and pressure  
 271 were used with Eq. ?? to calculate force, which was multiplied by moment arm to calculate torque values.

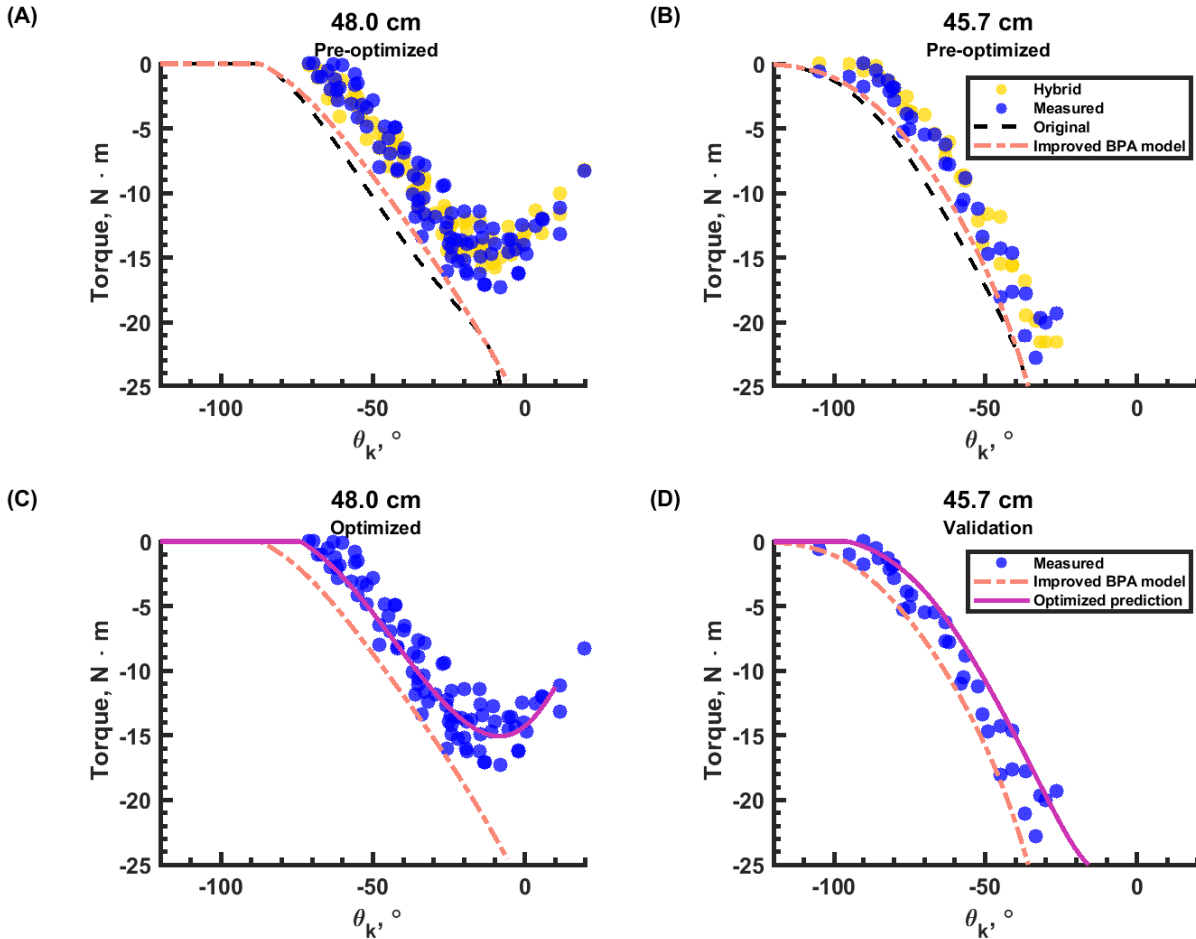


**Figure 6.** Results for the pinned knee joint using flexor BPAs. **(A)** Measured and pre-optimized torque prediction for the 48.0 cm BPA. **(B)** Measured and pre-optimized torque prediction for the  $l_{rest} = 45.7$  cm BPA. **(C)** Theoretical and measured torque for the  $l_{rest} = 48.0$  cm BPA using optimization results. **(D)** Predicted Measured torque for the  $l_{rest} = 45.7$  cm BPA using an optimization results

272 The magenta line represents the predicted torque, calculated with a new optimization parameter as described  
273 below.

274 Measured torque was slightly higher than the original model calculates for the 48 cm resting length BPA,  
275 while it was slightly lower than expected in the 45.7 cm BPA, and it was much lower in the 41.5 cm. The  
276 previous optimization results were not used with the extensor configuration. Firstly, by inspection, the zero  
277 point for the measured torque was shifted to the right of the original model, indicating an offset that was at  
278 least opposite in sign from the  $X_0$  term in the previous section. Secondly, if we look at the BPA 46 cm  $l_{rest}$   
279 as an example, we see good correlation between the hybrid-method calculated torque and the originally  
280 predicted torque, but a divergence in the actually measured torque.

281 This indicates that the source of error was not as much bracket deformation, but a phenomena that occurs  
282 as the BPA undergoes bending over the joint. The inner side of the BPA experiences less tensile stress than  
283 the outside, creating a force imbalance and a loss of part of the arc length of the BPA as usable length. We  
284 also noticed that the the more contracted a BPA was over the RoM, the less the torque results were affected  
285 by wrapping. We hypothesized that the an additional optimization term  $X_3$  should be introduced, such that

$$\Delta l = \begin{cases} X_3 R |\theta_{wrap} - \theta_k| \xi^2 & \theta_k \leq \theta_{wrap} \\ 0 & \theta_k \geq \theta_{wrap} \end{cases} \quad (14)$$

286 where  $\Delta l$  is the change in usable length of the BPA,  $R = 0.04$  m is the wrapping radius.  $\theta_{wrap} = -23$  deg  
 287 is the knee flexion angle when the BPA starts to bend over the knee joint, determined with solid modeling.  
 288  $\xi$  is the additive complement to relative strain, clamped between the values of 0 and 1, which yields

$$\xi = \begin{cases} 1 & \epsilon^* \leq 0 \\ 1 - \epsilon^* & 0 \leq \epsilon^* \leq 1 \\ 0 & \epsilon^* \geq 1 \end{cases} \quad (15)$$

289 Combining (15) into (14), and subtracting  $\Delta l$  from (13) yields

$$l_m = l_{LMT} - 2 l_{fitting} - l_{tsl} - X_0 - \Delta l \quad (16)$$

290 The optimization algorithm was again ~~gamultobj~~<sup>AIR spelling</sup> in Matlab. This time, the muscle origins bracket was  
 291 chosen. The bracket  $z_{br}$  axis is specified to be located on the anterior bracket surface, and coincident with  
 292 the line from the superior to the inferior anterior bolt axes. The  $y_{br}$  axis is parallel to the bolt hole, and the  
 293  $x_{br}$  axis is positive in the  $-Z$  direction. The optimization algorithm for this set solves for the best average  
 294 goodness-of-fit (GoF) measures RMSE, FVU, and maximum absolute residual for two BPAs, while the  
 295 third one was held out. Three rounds of optimization were performed, so that one of each of the BPAs  
 296 could be held out as validation. Then we picked the solution with the shortest distance between the average  
 297 GoF and the validation data, while also requiring improved GoF values for all the BPAs, with the exception  
 298 of maximum absolute residual on the  $l_{rest} = 48.0$  cm BPA.

299 Results are shown in Fig. 7. The solution was found while holding the  $l_{rest} = 41.5$  cm BPA for  
 300 validation. The optimization resulted in  $X_0 = -9.1$  mm,  $X_1 = 14.05$  kN m $^{-1}$  ( $x_{br}$  and  $z_{br}$  directions),  
 301  $X_2 = 178.9$  kN m $^{-1}$  ( $y_{br}$  direction), and  $X_3 = 0.2166$ . It should be noted here that the length offset  
 302  $X_0$  is almost equal in magnitude, but opposite sign, as the flexor configuration. The optimized torque  
 303 prediction for the  $l_{rest} = 48.0$  cm BPA has an RMSE = 0.8887, FVU = 0.2565, and a maximum absolute  
 304 residual of 2.4319 (Fig. 7A). For the  $l_{rest} = 45.7$  cm BPA, an RMSE = 0.5584, FVU = 0.0696, and a  
 305 maximum absolute residual of 1.3204 (Fig. 7B) were recorded. Finally, the  $l_{rest} = 41.5$  cm BPA has an  
 306 RMSE = 1.5809, FVU = 0.5062, and a maximum absolute residual of 2.9580 (Fig. 7C).

307 .

### 308 3.2.3 Extensor on Biomimetic Knee

309 We obtained results using the biomimetic knee with a  $\phi 10$  mm BPA in the extensor configuration. The  
 310 bracket frame origin was the centroid of the four bolts that hold the muscle origins bracket to the proximal  
 311 femur. The frame was rotated about  $Z$  so that  $x_{br}$  was pointed at the  $XY$  projection of the extensor muscle  
 312 origin location. The results for torque and relative strain are given in Fig. 8. The torque values measured  
 313 are significantly smaller than originally predicted (8A). Fig. 8B shows the length (using  $\epsilon^*$  as a proxy) is  
 314 very close to what we expected. Fig. 9 shows the difficulty of modeling a BPA path that passes through  
 315 the femoral condyles. Using the optimization results for extensor BPAs on the pinned knee joint, the

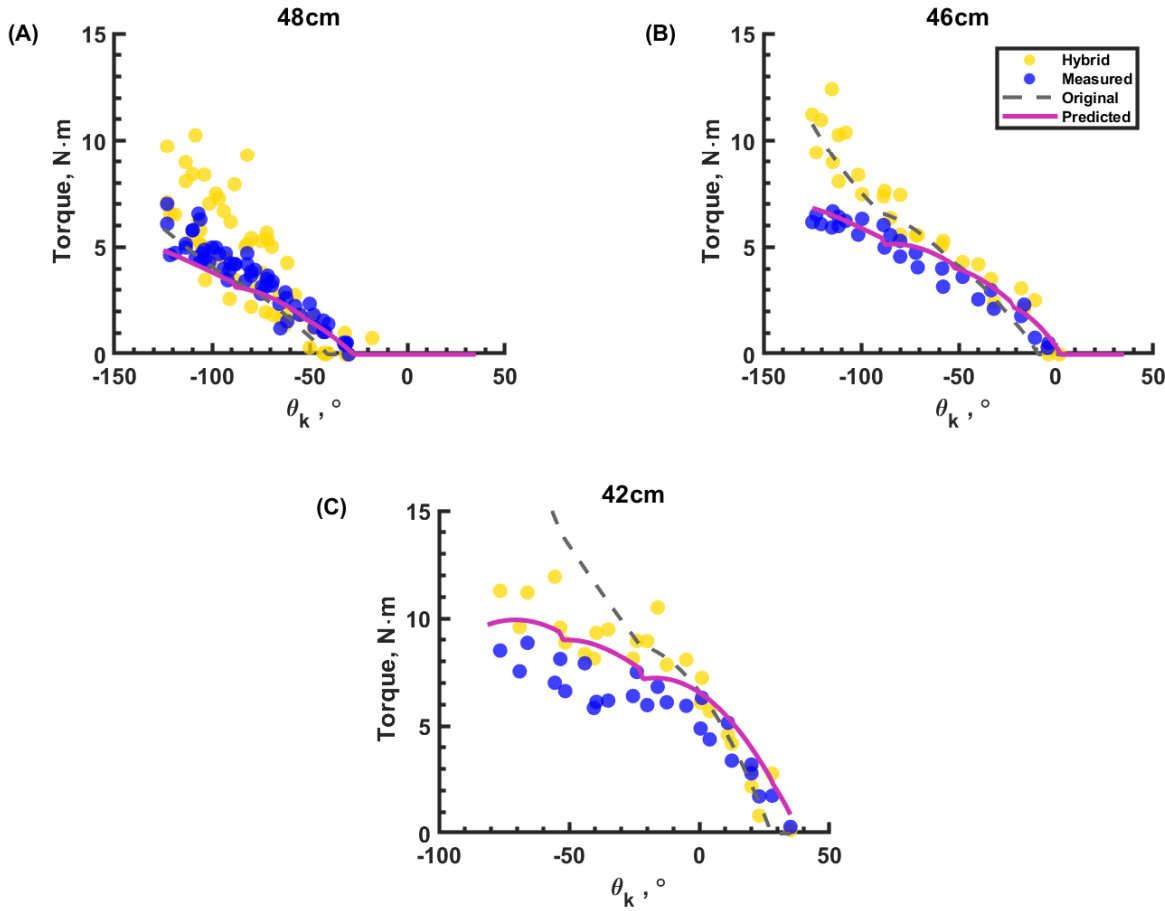


**Figure 7.** Pinned knee Torque with the extensor BPA for resting lengths, **(A)** 48.0 cm, **(B)** 45.7 cm, **(C)** and 41.5 cm.

316  $l_{rest} = 52.0$  cm BPA has an RMSE = 0.8920, FVU = 0.3396, and a maximum absolute residual of  
317 1.4188.

### 318 3.2.4 Flexor on Biomimetic Knee

319 Fig. 10 shows the isometric torque values of the biomimetic knee from measurements, the Hunt model  
320 (Hunt et al., 2017a), and the predictions of the updated model. The values for  $X_0$ ,  $X_1$ , and  $X_2$  from  
321 the flexors on the pinned knee were used. The bracket frame origin was the centroid of the four bolts  
322 that hold the muscle origins bracket to the proximal femur. The frame was rotated about  $Z$  so that  $x_{br}$   
323 was pointed at the  $XY$  projection of the flexor muscle origin location. Fig. 10A represents a  $\phi 10$  mm  
324  $l_{rest} = 41.5$  cm BPA with a 21 mm artificial tendon made out of  $\phi 1.5$  mm Shimano bicycle brake cable.  
325 The brake cable was wrapped four times. The BPA was pressurized to 604 kPa. The predicted values  
326 have an RMSE = 0.3007, FVU = 0.0102, and a maximum absolute residual of 0.4647 N · m. Fig. 10B  
327 represents a  $\phi 20$  mm  $l_{rest} = 41.5$  cm BPA with a 15 mm artificial tendon made out of Shimano bicycle  
328 brake cable (wrapped six times). Maximum human isometric torque values are shown as the black dotted  
329 line. The experiment was performed at 620 kPa and 325 kPa. At 620 kPa, the predicted values have an  
330 RMSE = 1.8024, FVU = 0.0499, and a maximum absolute residual of 3.5678 N · m. When the BPA  
331 pressure was reduced to 325 kPa, the predicted values have a fit of RMSE = 1.6712, FVU = 0.6835, and

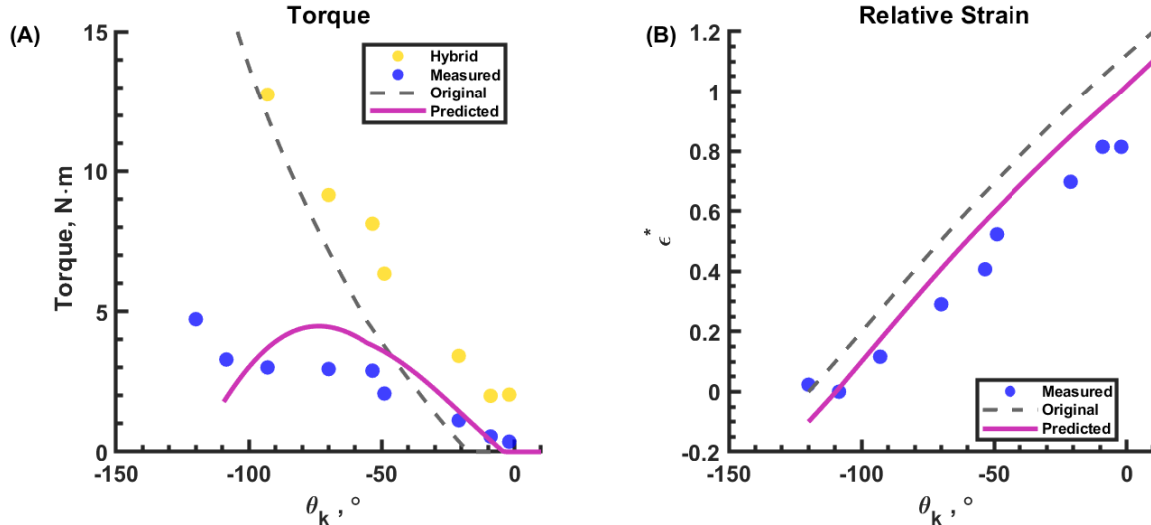


**Figure 8.** Measured versus expected results using a  $\phi 10$  mm,  $l_{rest} = 51.8$  cm extensor BPA on the biomimetic knee. (A) Isometric torque. Hybrid calculation in yellow (B) Relative contraction. Measured results are blue dots. Original prediction is a dashed black line. Optimized prediction is a solid magenta line.



**Figure 9.** A configuration that is particularly hard to model.

may be explaining why it is hard, & showing in Fig. 6.1 & Fig. 7.1  
concerning first skins before rendering could help give context.

332 a maximum absolute residual of  $3.0033 \text{ N} \cdot \text{m}$ . The BPA torque does not exceed the magnitude of the  
 333 human torque from ca.  $60 - 100$  degrees knee flexion. Allowing for a  $\pm 20\%$  deviation from the human  
 334 mean, the BPA does not produce human levels of torque from  $78 - 103$  degrees knee flexion.

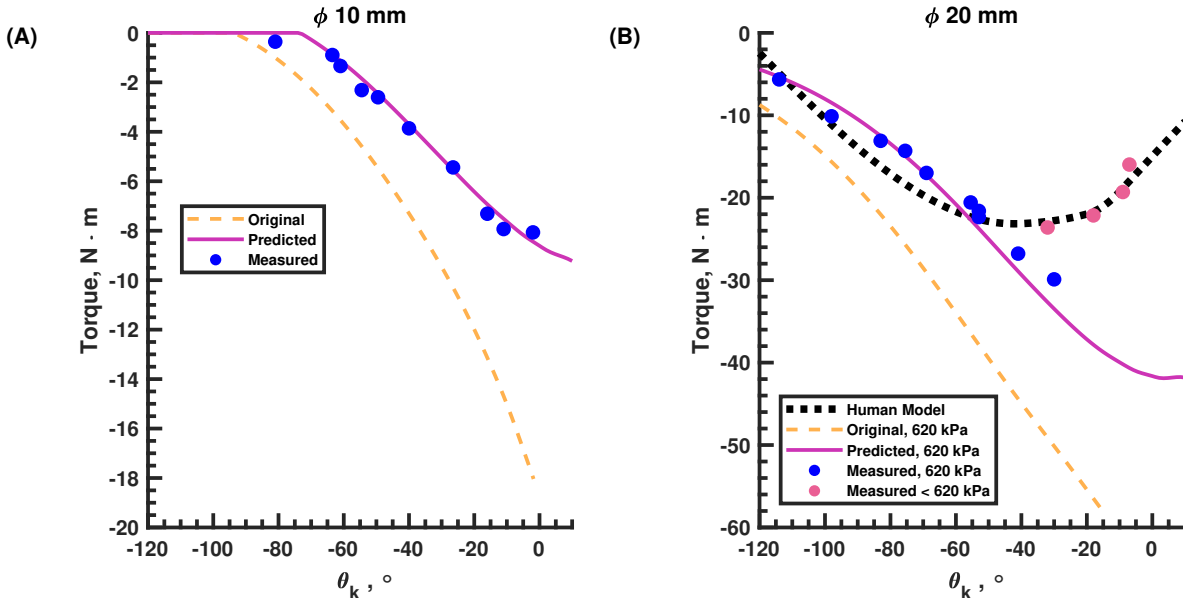


**Figure 10.** Biomimetic knee torque for (A)  $\phi 10 \text{ mm}$   $l_{rest} = 41.5 \text{ cm}$  flexor BPA with a 21 mm artificial tendon. Blue dots show the measured torque values. Magenta line is the predicted torque using the improved BPA characterization and optimization from the previous sections. The dashed light orange line shows the torque predicted using only the improved BPA characterization. (B)  $\phi 20 \text{ mm}$   $l_{rest} = 41.5 \text{ cm}$  flexor BPA with a 15 mm artificial tendon uses the same colors for 620 kPa results. Human values are given as a black dotted line. Due to the BPA exceeding the ultimate strength of the femur, torque measurements were taken at  $P < P_{max}$  to show the desired RoM is achievable. Results for torque measurements at 560 kPa, 421 kPa, 325 kPa and 281 kPa (from left to right, respectively), are shown as pink dots.

## 4 DISCUSSION

We have developed a  $F_{max}$  equations for 10 mm and 20 mm diameter Festo BPAs that does not currently exist in the literature. When examining Eq. 8 and measured data in Fig. 3B, it can be seen that as  $l_{rest}$  goes to infinity,  $F_{max,10}$  goes to 473.7 N. Festo data was queried at  $l_{rest} = 1$  m as an approximation of infinity. These data predict the  $\phi$ 10 mm BPA can produce  $F = 488.4$  N at  $P_{max}$ . Similarly, the Festo data predict a  $\phi$ 20 mm BPA will produce  $F = 1565.1$  N. However, our results for Eq. 9 show that  $F_{max,20}$  goes to 1461.8 N as  $l_{rest}$  approaches infinity. At long  $l_{rest}$ , the Festo data only overpredicts  $F$  by 3.2% in  $\phi$ 10 mm BPAs and 7.1% in  $\phi$ 20 mm BPAs.

The measured data shows unambiguously that as  $l_{rest}$  goes to zero, so does the force, whereas the Festo tool predicts exponential force growth (Fig. 3B and 3C). Perhaps more interestingly, when specifying  $l_{rest} = 100$  mm for the 10 mm and 20 mm diameter BPAs, the Festo predicted  $F_{max}$  is 507 N and 1862.5 N, respectively. However, using Eq. 8 and Eq. 9, the actual maximum forces are calculated to be 327.3 N and 853.7 N, respectively. Therefore, the error in the  $\phi$ 10 mm BPA is 54.9% and in the  $\phi$ 10 mm BPA it is 118.2%. Researchers using BPA resting lengths between 100 mm and 300 mm, like those working on DoggyDeux (Scharzenberger, 2019), should take note of these results.

It remains to be seen how  $\epsilon_{max}$  can be known a priori. We still suspect that it is a function of  $l_{rest}$ , but it might also be a function of product batch number, as well as total number of twists in the usable muscle area. Uncovering this relationship, if it exists in a meaningful way, will require controlled tests with technology that can take more accurate measurements. Not knowing this means there is still the potential for robots that go through long design stages to need a complete redesign if it is discovered that the robot does not produce the torque or have the RoM that the design team expects.

We have also introduced the concept of nondimensionalized isometric force that is a function of relative strain and relative pressure (Eq. 11). This elegant equation has only 3 coefficients and excellent goodness of fit values (Table 2). In the work presented here, we add in the relative pressure term,  $P^* = P/P_{620}$  (We note here that  $P_{620} = P_{max} = 620$  kPa is the maximum supply pressure for our system, and other users of this actuator may use a different supply pressure). Our data shows that by normalizing force, contraction, and pressure, we are able to create a simplified force equation as a function of contraction and pressure that scales well with initial actuator length, i.e.

$$F(\epsilon^*, P^*, l_{rest}) = F^*(\epsilon^*, P^*) \cdot F_{max}(l_{rest}) \quad (17)$$

For example, given  $l_{rest} = 54$  mm,  $P = 299.12$  kPa, the measured force was  $F_{actual} = 103.37$  N. Force prediction using only the Festo tool predicts the force to be  $F_{predict} = 270$  N. This is 161.2% greater than the measured force. Force prediction using function fit to Festo data (Table 2) using Festo data, and Eq. (17) gives  $F_{predict} = F^*(0, 0.4825) \cdot F_{max}(0.054) = 0.4873 \cdot 229.6$  N = 111.9 N. This is an error of 8.25%, which is much more accurate than using the Festo tool only.

The improved BPA characterization more accurately predicts isometric force produced by the BPAs. Unlike Eq. ??, it does not account for the hysteresis that occurs in BPAs. BPA artificial muscles are often said to be analogous to biological muscles because they have force length curves and can produce force only in tension. This analogy is worth closer inspection, although it should be kept in mind that biological muscle optimum fiber length  $l_{OFL}$  is not equivalent to  $l_{rest}$ . The improved Hill-muscle model of Thelen (2003) shows an exponential term for a muscle's passive force-length properties, and a squared

373 exponential term (gaussian) for the shape of the active force-length curve. Further characterization Festo  
 374 BPAs should include isokinetic and isotonic testing in both eccentric and concentric loading.

375 Our improved BPA characterization predicts torque more accurately than the original BPA model (see 6A  
 376 and 6B). This only accounts for part of the error. There are certainly many factors that affect the torque  
 377 results. Compliance in the testing system, position location tolerance, flexibility of brackets, imperfect path  
 378 modeling, and variation in individual BPAs are other factors.

379 Simplifying the model and testing it allowed us to see how we were deficient in our previous analysis.  
 380 The isometric system is not rigid. There is compliance in the winch cable, artificial tendons, and brackets  
 381 that bend and stretch. We introduced a constant length offset term  $X_0$ , axial stiffness  $X_1$ , and bending  
 382 stiffness  $X_2$ . The bracket frame of reference was placed where the rotated about  $z_b$ . Optimization found  
 383 results for a  $\phi 10$  mm BPA with  $l_{rest} = 48$  cm in the simple pinned knee configuration. These results were  
 384 validated with second  $\phi 10$  mm BPA with  $l_{rest} = 45.7$  cm.

385 The modeling of extensor BPA paths that wrap around the knee joint is an approximation with inherent  
 386 error (Fig. 9). When the moment arm is short, small changes to it can have a large effect on the resultant  
 387 torque (Young et al., 2019). It was assumed that wrapping the BPA around the joint would be easier to  
 388 account for than adding a patella, deterministically designing its location as a function of knee angle, and  
 389 accounting for friction. During greater magnitude knee flexion angles, shorter  $l_{rest}$  BPAs were noted as  
 390 being stretched and compressed (1B). The same force that caused the stretch and compression would also  
 391 sometimes cause the BPA to slip off of the anterior bolt head of the bolt that holds the femur to the knee.  
 392 This would result in a  $\pm 20$  mm displacement in the Z direction, which means a change the force vector and  
 393 a change in torque. The system designer, too, must be mindful. Fig. 7 shows a deviation between measured  
 394 and originally predicted results that widens as expected torque increases. This indicates system compliance.  
 395 However, the hybrid calculated torque matching or exceeding predicted torque, except for higher degrees  
 396 of flexion in the  $l_{rest} = 42$  mm, indicate a loss of functional  $l_m$ . BPA This is why the  $X_3$  term was created  
 397 (Eq. 14). Fig. 7 shows the improved fit from running the optimization that includes this term.

398 The biomimetic knee joint with an extensor BPA was used to validate the extensor optimization results.  
 399 The predicted line more closely matches the torque values. However, the results start to dip after more than  
 400 75 deg of knee flexion.

401 The analysis in this study has created novel equations for calculating force in Festo 10 mm and 20 mm  
 402 diameter BPAs. This study has elucidated the relationship between maximum BPA force  $F_{max}$  as a  
 403 function of resting length  $l_{rest}$  (Eq. 8, Eq. 9, Table 1). Very accurate equations for the nondimensionalized  
 404 force in a BPA as a function of relative strain  $\epsilon^*$  and relative pressure  $P^*$ , (Eq. 11 and Table 2). In the  
 405 presented nonlinear biomimetic robotic system, rigid body mechanics simplifications, often encountered in  
 406 other robotic and biomechanical systems, are removed. Instead, working from the simple to the complex  
 407 elucidated mechanisms of system compliance that will lead to much more accurate first iteration designs.  
 408 Technologies have been developed to predict system bending and axial compliance, a constant length offset,  
 409 and a loss of usable length that occurs as a muscle bends around a joint.

## RESOURCE IDENTIFICATION INITIATIVE

- 410 • MATLAB (RRID:SCR\_001622)  
411 • OpenSim (RRID:SCR\_002683)  
412 • Arduino UNO (RRID:SCR\_017284)

## CONFLICT OF INTEREST STATEMENT

413 The authors declare that the research was conducted in the absence of any commercial or financial  
414 relationships that could be construed as a potential conflict of interest.

## AUTHOR CONTRIBUTIONS

415 BB, CM, and AH contributed to the conception and design of the study. BB and CM wrote the code to  
416 calculate theoretical isometric torque values of the robot. Figures were created by BB. BB, LB, LP, and  
417 ME wrote code for data collection and analysis. BB, LP, and ME collected the data. BB performed the  
418 statistical analysis and organized the database. BB wrote the first draft of the manuscript. BB, LB, and AH  
419 wrote sections of the manuscript. All authors read the manuscript, contributed to its revision, and approved  
420 the submitted version.

## FUNDING

421 Research for this article was funded by the Department of Mechanical and Materials Engineering at  
422 Portland State University, the National Science Foundation (NSF) grant for NeuroNex: Communication,  
423 Coordination, and Control in Systems (C3NS) 2015317 and NSF grant 1943483.

## ACKNOWLEDGMENTS

424 The authors would like to acknowledge the contribution of Alex Steele, who designed the initial biomimetic  
425 4-bar knee linkage we used for the test. He gave us solid models, built a 3D prototype, and let us break said  
426 prototype. His prompt and thoughtful responses to our questions about the previous design was very much  
427 appreciated. The authors would also like to thank Jasmine Bradley for her help reworking the figures in the  
428 results section. As a visual designer, her contributions improved the aesthetic quality of the images. She  
429 also helped us choose colors that ensured data accessibility for people with color blindness.

## SUPPLEMENTAL DATA

430 Supplemental Data includes figures for the test setup.

## DATA AVAILABILITY STATEMENT

431 The data sets are available from the authors upon reasonable request.

## REFERENCES

- 432 Asano, Y., Okada, K., and Inaba, M. (2017). Design principles of a human mimetic humanoid: Humanoid  
433 platform to study human intelligence and internal body system. *Science Robotics* 2. doi:10.1126/  
434 scirobotics.aaq0899. Publisher: Science Robotics Section: Research Article
- 435 Asano, Y., Okada, K., and Inaba, M. (2019). Musculoskeletal design, control, and application of human  
436 mimetic humanoid Kenshiro. *Bioinspiration & Biomimetics* 14, 036011. doi:10.1088/1748-3190/ab03fc
- 437 Bolen, B. P. and Hunt, A. J. (2019). Determination of Artificial Muscle Placement for Biomimetic  
438 Humanoid Robot Legs. In *Biomimetic and Biohybrid Systems*, eds. U. Martinez-Hernandez, V. Vouloutsi,  
439 A. Mura, M. Mangan, M. Asada, T. J. Prescott, and P. F. Verschure (Cham: Springer International  
440 Publishing), vol. 11556. 15–26. doi:10.1007/978-3-030-24741-6\_2
- 441 Delp, S., Loan, J., Hoy, M., Zajac, F., Topp, E., and Rosen, J. (1990). An interactive graphics-based model  
442 of the lower extremity to study orthopaedic surgical procedures. *IEEE Transactions on Biomedical  
443 Engineering* 37, 757–767. doi:10.1109/10.102791
- 444 Delp, S. L., Anderson, F. C., Arnold, A. S., Loan, P., Habib, A., John, C. T., et al. (2007). OpenSim:  
445 Open-Source Software to Create and Analyze Dynamic Simulations of Movement. *IEEE Transactions  
446 on Biomedical Engineering* 54, 1940–1950. doi:10.1109/TBME.2007.901024
- 447 [Dataset] Festo (2022). Festo Fluidic Muscle DMSP
- 448 Goldsmith, C. A., Quinn, R. D., and Szczecinski, N. S. (2021). Investigating the role of low level  
449 reinforcement reflex loops in insect locomotion. *Bioinspiration & Biomimetics* 16, 065008. doi:10.1088/  
450 1748-3190/ac28ea. Publisher: IOP Publishing
- 451 Hunt, A., Graber-Tilton, A., and Quinn, R. (2017a). Modeling length effects of braided pneumatic  
452 actuators. In *Volume 5A: 41st Mechanisms and Robotics Conference* (Cleveland, OH: ASME), vol.  
453 58172, V05AT08A008. doi:10.1115/detc2017-67458
- 454 Hunt, A., Szczecinski, N., and Quinn, R. (2017b). Development and Training of a Neural Controller for  
455 Hind Leg Walking in a Dog Robot. *Frontiers in Neurorobotics* Volume 11 - 2017. doi:10.3389/fnbot.  
456 2017.00018
- 457 Ijspeert, A. J. (2020). Amphibious and Sprawling Locomotion: From Biology to Robotics and  
458 Back. *Annual Review of Control, Robotics, and Autonomous Systems* 3, 173–193. doi:10.1146/  
459 annurev-control-091919-095731. eprint: <https://doi.org/10.1146/annurev-control-091919-095731>
- 460 [Dataset] Lang, R. (2005). Festo MuscleSim
- 461 Martens, M. and Boblan, I. (2017). Modeling the Static Force of a Festo Pneumatic Muscle Actuator: A  
462 New Approach and a Comparison to Existing Models. *Actuators* 6, 33. doi:10.3390/act6040033
- 463 Morrow, C., Bolen, B., and Hunt, A. (2020). Optimization of Artificial Muscle Placements for a Humanoid  
464 Bipedal Robot. In *Biomimetic and Biohybrid Systems* (Springer, Cham), vol. 12413 of *Lecture Notes in  
465 Computer Science*, 257–269. doi:10.1007/978-3-030-64313-3\_25
- 466 Scharzenberger, C. W. (2019). *Design of a Canine Inspired Quadruped Robot as a Platform for Synthetic  
467 Neural Network Control*. Master's thesis, Portland State University, Digital
- 468 Schilling, M., Paskarbeit, J., Ritter, H., Schneider, A., and Cruse, H. (2022). From Adaptive Locomotion  
469 to Predictive Action Selection – Cognitive Control for a Six-Legged Walker. *IEEE Transactions on  
470 Robotics* 38, 666–682. doi:10.1109/TRO.2021.3106832. Conference Name: IEEE Transactions on  
471 Robotics
- 472 Seth, A., Hicks, J. L., Uchida, T. K., Habib, A., Dembia, C. L., Dunne, J. J., et al. (2018). OpenSim:  
473 Simulating musculoskeletal dynamics and neuromuscular control to study human and animal movement.  
474 *PLOS Computational Biology* 14, e1006223. doi:10.1371/journal.pcbi.1006223

- 475 Shin, H., Ikemoto, S., and Hosoda, K. (2018). Constructive understanding and reproduction of functions  
476 of gluteus medius by using a musculoskeletal walking robot. *Advanced Robotics* 32, 202–214. doi:10.  
477 1080/01691864.2018.1434015. Publisher: Taylor & Francis
- 478 Steele, A. G. (2018). *Biomimetic Design and Construction of a Bipedal Walking Robot*. Thesis, Portland  
479 State University, Portland, Oregon, USA
- 480 Steele, A. G., Hunt, A., and Etoundi, A. C. (2017). Development of a Bio-inspired Knee Joint Mechanism  
481 for a Bipedal Robot. In *Biomimetic and Biohybrid Systems* (Springer, Cham), Lecture Notes in Computer  
482 Science, 418–427. doi:10.1007/978-3-319-63537-8\_35
- 483 Steele, A. G., Hunt, A., and Etoundi, A. C. (2018). Biomimetic Knee Design to Improve Joint Torque and  
484 Life for Bipedal Robotics. In *Towards Autonomous Robotic Systems*, eds. M. Giuliani, T. Assaf, and  
485 M. E. Giannaccini (Cham: Springer International Publishing), 91–102
- 486 Sárosi, J., Piteľ, J., Tóthová, M., Hošovský, A., and Bíró, I. (2017). COMPARATIVE SURVEY  
487 OF VARIOUS STATIC AND DYNAMIC MODELS OF PNEUMATIC ARTIFICIAL MUSCLES.  
488 *Transactions of the Canadian Society for Mechanical Engineering* 41, 825–844. doi:10.1139/  
489 tcsme-2017-514
- 490 Thelen, D. G. (2003). Adjustment of Muscle Mechanics Model Parameters to Simulate Dynamic  
491 Contractions in Older Adults. *Journal of Biomechanical Engineering* 125, 70–77. doi:10.1115/1.  
492 1531112
- 493 Wu, G. and Cavanagh, P. (1995). FOR STANDARDIZATION IN THE REPORTING OF KINEMATIC  
494 DATA. *Journal Biomechanics* 28, 1257–1261. doi:0021-9290(95)00017-8
- 495 Wu, G., Siegler, S., Allard, P., Kirtley, C., Leardini, A., Rosenbaum, D., et al. (2002). ISB recommendation  
496 on definitions of joint coordinate system of various joints for the reporting of human joint motion—part  
497 I: ankle, hip, and spine. *Journal of Biomechanics* 35, 543–548. doi:10.1016/S0021-9290(01)00222-6
- 498 Young, F., Rode, C., Hunt, A., and Quinn, R. (2019). Analyzing Moment Arm Profiles in a Full-Muscle  
499 Rat Hindlimb Model. *Biomimetics* 4, 10. doi:10.3390/biomimetics4010010

## FIGURES

## TABLES

**Table 1.** Maximum force equations with coefficient values and goodness-of-fit measures. Eq. 10 is compared to data taken at 620 kPa. Eq. 8 and Eq. 9 are compared against maximum force from using the Festo tool. It was not necessary to fit an adjusted  $R^2$  in this case.

Equation	Coefficient	CI (95%)	Model			Comparison		
			Adj. $R^2$	RMSE	Max. Error	Adj. $R^2$	RMSE	Max. Error
10	$a_1 = 0.4895 \text{ N kPa}^{-1}$	(0.4822, 0.4968)	0.9945	11.61 N	55.3 N	0.9854	14.7 N	30.9 N
	$a_2 = 0.03068 \text{ kPa}^{-1} \text{ m}^{-1}$	(0.0282, 0.03317)						
8	$b_1 = 303.5 \text{ N}$	(300, 308)	0.9854	14.72 N	30.9 N	–	189.9 N	375.6 N
	$b_2 = 19.03 \text{ m}^{-1}$	(17.48, 20.57)						
9	$b_1 = 922.4 \text{ N}$	(914.2, 930.7)	0.9945	23.83 N	62.1 N	–	668.4 N	1590.1 N
	$b_2 = 15.37 \text{ m}^{-1}$	(14.75, 15.98)						

**Table 2.** Normalized isometric BPA force equation (Eq. 11) coefficient values and goodness-of-fit measures.

BPA dia., data source	Coefficient	CI (95%)	Model			Validation		
			Adj. $R^2$	RMSE	Max. Error	Adj. $R^2$	RMSE	Max. Error
$\phi 10 \text{ mm, Festo}$	$c_0 = 0.3976$	(0.3753, 0.42)	0.9948	0.0258	6.9%	0.9882	0.03877	14.4%
	$c_1 = 6.482$	(6.022, 6.943)						
	$c_2 = 0.998$	(0.9238, 1.072)						
$\phi 10 \text{ mm, Experiment}$	$c_0 = 0.5822$	(0.5742, 0.5902)	0.9998	0.0045	10.6%	0.9878	0.03966	11.4%
	$c_1 = 4.142$	(4.043, 4.241)						
	$c_2 = 0.5368$	(0.5235, 0.55)						
$\phi 20 \text{ mm, Festo}$	$c_0 = 0.2165$	(0.1922, 0.2408)	0.9952	0.0199	3.8%	0.9904	0.02626	7.6%
	$c_1 = 7.583$	(6.557, 8.609)						
	$c_2 = 1.515$	(1.384, 1.646)						
$\phi 20 \text{ mm, Experiment}$	$c_0 = 0.2607$	(0.2442, 0.2773)	0.9927	0.0229	6.9%	0.995	0.02019	6.5%
	$c_1 = 6.398$	(5.584, 7.212)						
	$c_2 = 1.303$	(1.228, 1.378)						